Microwave spectroscopy of heliumlike Rydberg states of H_2 and D_2: Determinations of the dipole polarizabilities of H_2^+ and D_2^+ ground states

P. L. Jacobson, R. A. Komara, W. G. Sturrus,* and S. R. Lundeen
Department of Physics, Colorado State University, Fort Collins, Colorado 80523
(Received 8 February 2000; published 15 June 2000)

The fine-structure intervals separating the highest-L, $n=9$ and 10 Rydberg states of H_2 and D_2 bound to the $\nu=0$, $R=0$ ground states of H_2^+ and D_2^+ have been measured precisely with microwave spectroscopy and used to deduce the isotropic dipole polarizabilities of the ground states of both these ions. The results, $\alpha_S(H_2^+)=3.167\,96(15)a_0^3$ and $\alpha_S(D_2^+)=3.071\,87(54)a_0^3$, agree with *a priori* theory to within about 0.02%, but the H_2^+ result indicates that the theory is incomplete at this level.

PACS number(s): 33.15.Kr, 33.15.Pw, 33.20.Bx

I. INTRODUCTION

Microwave spectroscopy of high-L Rydberg states of H_2 has proven to be an important source of information about the H_2^+ ion. In these studies, the weakly bound and nonpenetrating Rydberg electron acts as a sensitive probe of the electric and magnetic properties of the ion binding it in its orbit. Studies of Rydberg states bound to the $\nu=0$, $R=1$ state of H_2^+ have resulted in measurements of the quadrupole moment and dipole polarizabilities [1] and hyperfine constants [2] of that state, as well as a determination of the rotational energy interval separating it from the $\nu=0$, $R=3$ state of H_2^+ [3]. All these measurements have been precise enough to stimulate improved calculations [4] which, except in the case of the H_2^+ hyperfine constants, give good agreement with the measurements. Recently, a study of high-L Rydberg states of H_2 and D_2 bound to the $\nu=0$, $R=0$ ground states of H_2^+ and D_2^+ was reported, which led to a determination of the dipole polarizabilities of both ion ground states [5]. That study has now been extended, and this paper reports its final results. Five additional fine-structure intervals have been measured, and those reported earlier have been improved in precision. This makes a total of 15 fine-structure intervals, eight in H_2 and seven in D_2. The wider pattern of improved data gives higher confidence in the determinations of α_S. In addition, the calculations of higher-order contributions to the fine structure, which appear as corrections in the analysis by which the polarizabilities are deduced, have been improved, reducing their contribution to the uncertainty in the polarizabilities. Together, these two improvements lead to a reduction in the uncertainty of α_S by as much as a factor of 5 over the initial report. A number of improved calculations of α_S have appeared since the initial report, providing a timely comparison with the new measurements. The completed experiment is described in detail below, along with a full discussion of the data analysis leading to the determination of the polarizabilities.

The high-L Rydberg states of H_2 (or D_2) differ qualitatively from lower-L Rydberg states of the same molecules because of the extremely weak coupling between the nonpenetrating high-L electron and the ion core. The high-L eigenstates are very close to the zeroth-order description, which characterizes the system by the quantum numbers of the free ion core (ν,R), the hydrogenic Rydberg electron (n,L), and the additional quantum number N, which gives the total angular momentum of the system (exclusive of spin),

$$\vec{N}=\vec{R}+\vec{L},$$

where R and L are the separate angular momenta of the ion core and Rydberg electron, respectively.

Deviations from this zeroth-order description are described by an effective potential [1],

$$\begin{aligned}V_{\rm eff}(\vec{\rho},\vec{r})=&-\frac{Q(\rho)}{r^3}P_2(\cos\theta)-\frac{1}{r^4}\\&\times\left(\frac{\alpha_S(\rho)}{2}+\frac{\alpha_T(\rho)}{3}P_2(\cos\theta)\right)-\frac{\Phi(\rho)}{r^5}\\&\times P_4(\cos\theta)-\frac{1}{r^6}\left(\frac{C_0(\rho)}{10}+\frac{C_1(\rho)}{7}\right.\\&\left.\times P_2(\cos\theta)+\frac{12C_2(\rho)}{35}P_4(\cos\theta)\right)\\&+\frac{1}{r^6}\left[\tfrac{3}{2}\,\beta_S(\rho)+\tfrac{1}{2}\,\beta_T(\rho)P_2(\cos\theta)\right]\\&-\frac{1}{r^6}\left(\frac{E_1(\rho)}{7}P_2(\cos\theta)+\frac{E_2(\rho)}{35}P_4(\cos\theta)\right)\\&+\cdots,\end{aligned}\tag{1}$$

where $\vec{\rho}$ is the internuclear axis of the H_2^+ ion, $\vec{r}$ is the coordinate of the Rydberg electron relative to the ion's center of mass, θ is the angle between $\vec{\rho}$ and $\vec{r}$, and all terms are in atomic units. $V_{\rm eff}$ has no dependence on the coordinate of the inner electron, but depends implicitly on this electron through the parameters that appear as coefficients in $V_{\rm eff}$. In addition, Q is the quadrupole moment, α_S,α_T are the scalar and tensor adiabatic dipole polarizabilities, Φ is the hexadecapole moment, C_0,C_2,C_4 are the adiabatic quadrupole po-

*Permanent address: Dept. of Physics and Astronomy, Youngstown State University, Youngstown, OH 44555.

larizabilities, β_S, β_T are the scalar and tensor nonadiabatic dipole polarizabilities, and E_1, E_2 are the adiabatic dipole-octupole polarizabilities. The Rydberg fine structure can be described by a perturbation expansion in V_{eff}:

$$E(\nu,R,n,L,N) = E^{[0]}(\nu,R,n) + E^{[1]}(\nu,R,n,L,N) + E^{[2]} \times(\nu,R,n,L,N) + E^{[3]}(\nu,R,n,L,N) + \cdots . \tag{2}$$

The zeroth-order energy $E^{[0]}$ does not contribute to the fine structure since all states of common ν,R,n are degenerate in this order. For states with $R=0$, such as those studied here, only the scalar terms in V_{eff} contribute to $E^{[1]}$, and these produce a fine-structure pattern consisting of a single eigenstate for each value of L. Except for its scale, this pattern is similar to the fine structure of atomic helium, and so we refer to these Rydberg states of H_2 and D_2 as ''heliumlike.'' For high-L levels, the contribution of successive scalar terms in V_{eff} decreases rapidly as the inverse power of r increases, and the leading term, proportional to α_S, dominates the fine-structure pattern. The higher-order perturbation energies $E^{[2]}$ and $E^{[3]}$ are generally small corrections to the structure. Our approach in this experiment is to find, from the experimentally measured intervals, an estimate of the energy intervals due to $E^{[1]}$ alone, by subtracting calculated contributions of $E^{[2]}$ and $E^{[3]}$ and relativistic corrections from the measured intervals. The variation of $\Delta E^{[1]}$ with L can then be used to separate out the leading contribution and determine α_S.

II. EXPERIMENTAL TECHNIQUE

The Rydberg fine-structure measurements reported here are obtained using techniques similar to those used in past H_2 [1] and helium [6] fine-structure measurements. A fast Rydberg beam is obtained by charge transfer from an accelerated beam of H_2^+ or D_2^+ ions. Specific fine-structure levels in the fast beam are detected by a three-step process consisting of (1) resonant excitation to a very highly excited state using a Doppler-tuned CO_2 laser, (2) Stark ionization of the highly excited state, and (3) collection of the resulting ion current. Direct fine-structure transitions are induced with rf electric fields and detected by the consequent change in population of the detected fine-structure level and the associated ion current. Figure 1 shows a schematic diagram of the major components of the apparatus, along with a generic level diagram describing the experiment.

A number of apparatus improvements were made for this experiment which greatly improved the signal-to-noise (S/N) ratio over past H_2 measurements [1]. These included the following.

(1) Use of a Cs vapor charge-exchange cell [7] instead of a simple gas charge-exchange cell. This improves the fraction of the Rydberg population that is formed in the detected $n=9$ and 10 levels.

(2) Use of a two-stage preionizer after the charge-exchange cell. The purpose of the preionizer is to reduce the population of the very highly excited states that would otherwise contribute to a background ion current and degrade

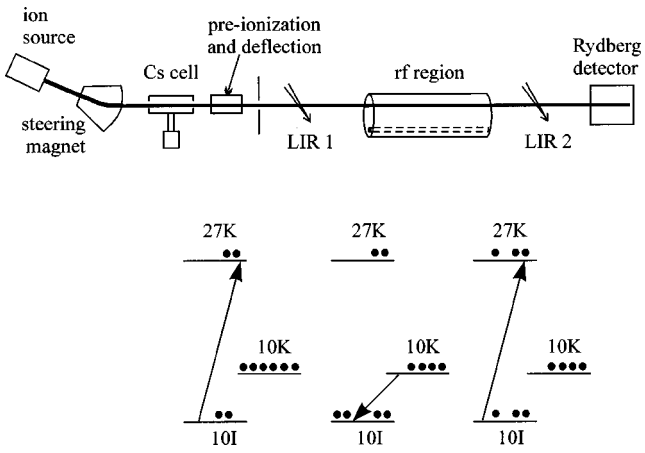

FIG. 1. Schematic diagram showing the major components of the apparatus. The incident ion beam (H_2^+ or D_2^+) is neutralized in the Cs vapor cell. A region of strong electric field removes any remaining ions and also Stark-ionizes Rydberg electrons in weakly bound states. Two CO_2 lasers, LIR1 and LIR2, drive transitions upward from $n=9$ or 10 to a weakly bound level. The region of rf electric field causes transitions between fine-structure levels of the same n. Finally, the Rydberg detector Stark-ionizes and collects any weakly bound levels. The level diagram below illustrates the sequence of population transfers used to observe the resonance signal corresponding to the $10I$-$10K$ transition.

the S/N ratio for the fine-structure measurement. In previous studies, it was noted that a single-stage preionizer was less effective in reducing background for a H_2 beam than for a helium beam. Presumably this is because of repopulation of highly excited Rydberg levels after ionization resulting from transfer of rovibrational energy into electronic excitation, a process that has been studied elsewhere [8]. Our two-stage preionizer consists of two short regions of strong longitudinal electric field, separated by a region of zero field. With this device, we observed background ion current comparable to that obtained with an atomic helium beam.

(3) Use of an improved Rydberg ionizer/detector. This device consists of two regions of longitudinal field with a 3:1 field strength ratio. This design ionizes, at a specific location in space, all Rydberg levels that Stark ionize over a factor of 3 in field strength. The potential at that location (V_s) results in an energy boost to these ions which allows them to be separated from ions produced in other ways, such as collisional ionization along the beam path. Following the ionizer, an einzel lens focuses the signal ions and deflection fields steer them into a Channeltron electron multiplier. For tuning purposes, these deflection fields can be reversed, and the signal focus adjusted while the signal ions are viewed on a beam viewer (Colutron BVS-1). The entire detector is mounted inside a 10-in. conflat tee, and maintained at a pressure of less than 1×10^{-8} Torr. This reduces background ions which are otherwise produced by collisional ionization of neutral molecules close to the point where Stark ionization occurs.

The first step in studying the Rydberg fine structure is obtaining CO_2 excitation spectra that resolve the fine structure of the states in question. Figure 2 shows typical ex-

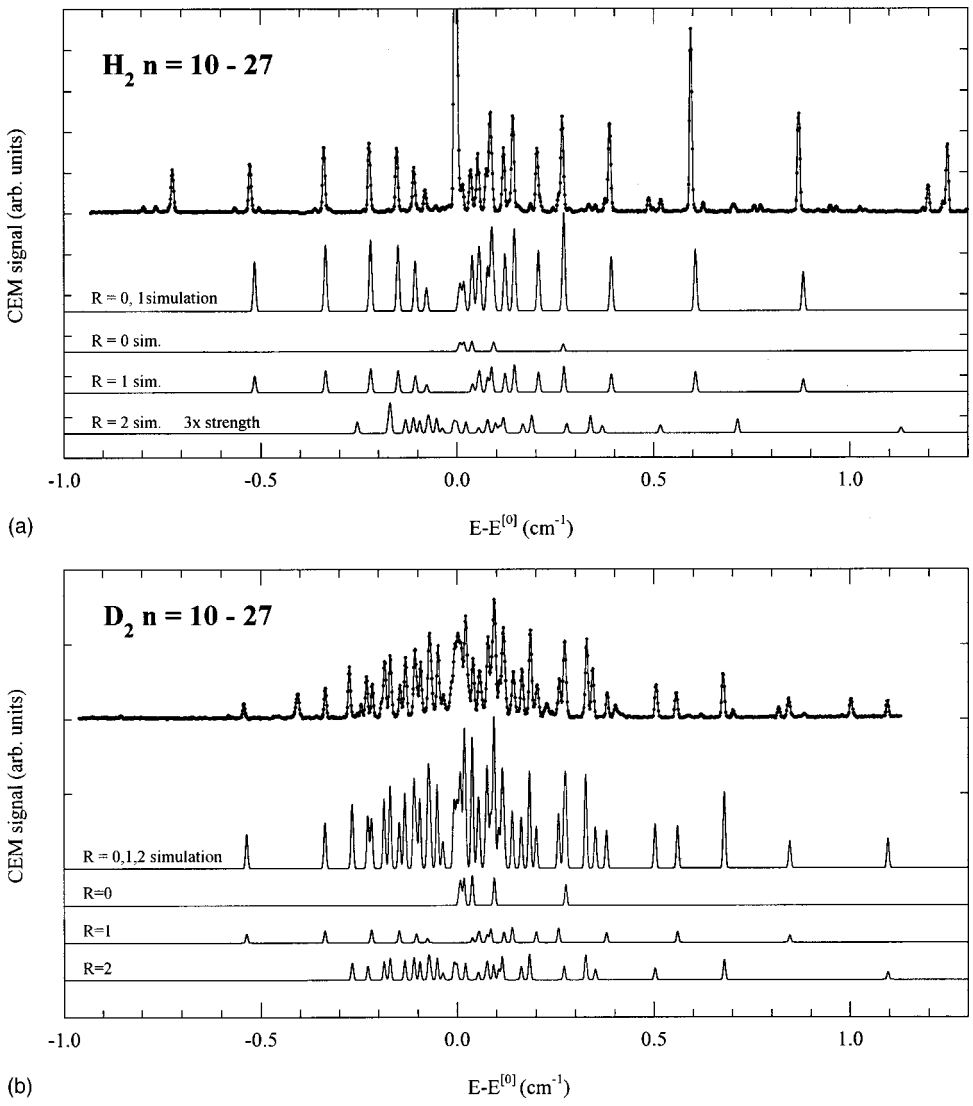

FIG. 2. (a) Laser excitation spectrum corresponding to 10-27 transitions in H_2. The vertical axis is the Stark-ionized current measured in the Rydberg detector. The horizontal axis is the difference between the Doppler-tuned CO_2 laser frequency and the zeroth-order transition frequency (946.584 cm^{-1}). (b) Laser excitation spectrum corresponding to 10-27 transitions in D_2. As in 2(a) the horizontal axis is the difference between the Doppler-tuned CO_2 laser frequency and the zeroth-order transition frequency, but in this case, the zeroth-order frequency is 946.713 cm^{-1} because of reduced mass corrections.

amples of such optical spectra for H_2 and D_2. Below the experimental spectra are shown simulated spectra based on the calculated fine structure and an assumed pattern of relative line intensities. All the lines identified in the spectra come from Rydberg levels that are bound to ground vibrational states of the core ions. Vibrationally excited states are expected to rapidly autoionize after charge capture, and so are not expected to appear in the spectrum. As an aid to interpreting the spectra, the simulation shown in Fig. 2 separates the contributions of $R=0,1,2$ levels. A striking difference between the H_2 and D_2 spectra is that the $R=1$ levels dominate the H_2 spectrum, but $R=0$ and 2 levels dominate the D_2 spectrum. It was because of the weakness of the $R=0$ lines in H_2 that no $R=0$ lines were conclusively identified in the initial reports of H_2 spectra of this type [9]. Even with the higher S/N ratio of the present measurement, the $R=0$ lines are not completely resolved in the H_2 spectrum. By contrast, in the D_2 spectrum, the $R=0$ lines are among the strongest lines in the spectrum. The difference in relative line intensities in the two spectra is due to nuclear statistics. H_2^+ contains two spin-$\frac{1}{2}$ fermions which must be in an antisymmetric state. Consequently, the even-R levels have $I=0$, while the odd-R levels have $I=1$. This gives the odd-R levels a 3:1 advantage in statistical weight in H_2. D_2^+, however, contains two spin-1 bosons which must be in a symmetric state. Thus, in D_2^+ the even-R levels have $I=0$ or 2 and the odd-R levels have $I=1$, giving the even-R levels a 6:3 advantage in statistical weight. In spite of the difference in relative intensities in the two spectra, the $R=0$ lines are actually weaker in the D_2 spectra. In other words, even the largest signals for D_2 are smaller than the weak $R=0$ lines for H_2. The reason for this is the much larger number of D_2^+ states populated in the ion source. The $\nu=0$ fraction is estimated to be about 9.0% for H_2^+ and 3.3% for D_2^+ [10]. Within the $\nu=0$ states, the $R=0$ fraction, as estimated from a room-temperature Boltzmann distribution including the nuclear statistics factor, is about 23% for H_2^+ and 45% for D_2^+. Here the factor of 6 statistical advantage of $R=0$ states in D_2^+ is largely compensated by the smaller rotational interval and the consequent higher degree of rotational excitation. When the smaller $v=0$ population fraction is also included, the fact that the D_2 $R=0$ lines are weaker than the H_2 $R=0$ lines is in agreement with estimates.

Precision spectroscopy of the fine-structure intervals is obtained by using one of the optical resonance lines as a detector of rf-induced transitions directly between fine-structure levels of the same n. For example, Fig. 2 shows an $R=0$ line at $E-E^0=0.09\,\mathrm{cm}^{-1}$ in the D_2 10-27 excitation spectrum, which by comparison with the simulation is identified as the $(0,0)10H_5$-$(0,0)27I_6$ transition. Since the $n=27$ levels have been emptied by the preionizer, the strength of this signal is proportional to the population of the $(0,0)10H_5$ Rydberg state of D_2. If, prior to this laser excitation, the D_2 beam encounters a rf electric field whose frequency matches the transition to either of the two neighboring $n=10$ fine-structure levels satisfying the $\Delta L=\mp 1$ selection rule, the rf-induced fine-structure transition can change the population of the $(0,0)10H_5$ level and the resulting optical signal strength. Measuring the strength of the optical signal as a function of the rf frequency gives a way to detect direct fine-structure transitions. Since the interaction time with the rf electric field is many times longer than the interaction time with the CO_2 laser, the resolution obtained with the direct rf spectroscopy is many times greater than with the optical spectroscopy. With this method, the size of the rf signal is proportional to the initial population difference between the two coupled levels. In order to ensure that such a population difference exists, an initial laser interaction region (LIR1) is used to deplete the population of one of the two levels involved in the transition. The sequence of optical and rf transitions used to observe a typical signal, the $10I$-$10K$, is illustrated schematically in Fig. 1.

Four different rf interaction regions were used in this study. The geometry of each region is illustrated in Fig. 3. Three of the regions, *A*, *B*, and *C*, were 50-Ω TEM transmission lines of various geometries. In these regions, the rf electric field propagates with a velocity c either parallel or antiparallel to the Rydberg beam. The ×'s in Fig. 3 indicate the approximate position of the Rydberg beam within the cross section of the transmission lines. Regions *A* and *B* were about 1 m in length, while region *C* was about 30 cm. A fourth region *D* consisted of an 80-cm length of *G*-band waveguide. The limited frequency range of each of the regions, indicated in Fig. 3, made it necessary to use all four to access the transitions of this study.

The initial identification of the $R=0$ lines in the spectra is made by comparison with the simulated spectra. In many cases, the $R=0$ lines are not fully resolved, but are blended with other lines. After a rf resonance is found, the location of the relevant optical lines can be confirmed free of the overlapping lines by measuring the rf resonance size as a function of the two laser tunings. Once the tuning of both LIR1 and LIR2 is optimized for the size of the rf signal, the signal is measured repeatedly and averaged to obtain the best possible S/N ratio. Figure 4 shows typical resonance shapes for the $9K$-$9L$ transitions in both isotopes. Another typical signal, the $9I$-$9K$, was illustrated in our earlier report [5].

The resonances of Fig. 4 show the influence of unresolved spin structure on the resonance shape. This structure is due to a combination of the hyperfine interactions in the ion core and the magnetic and exchange interactions between the two

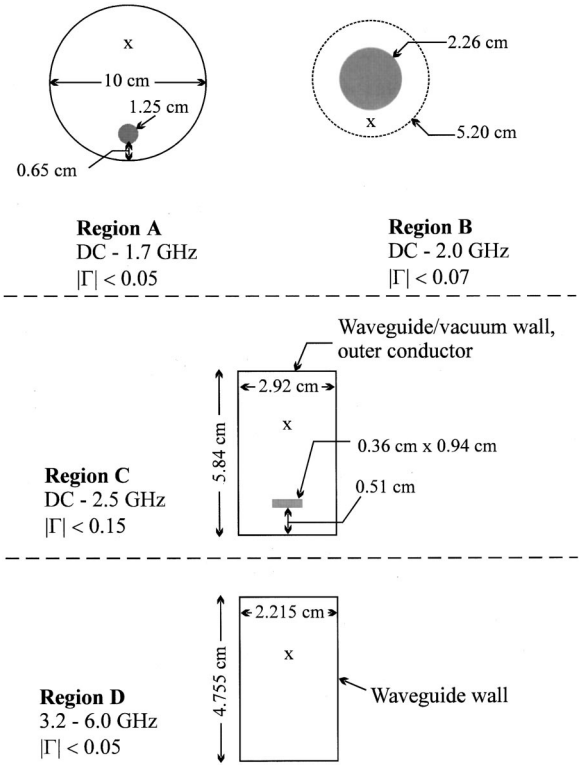

FIG. 3. Cross-sectional geometries of the several rf regions used in this experiment. Regions *A*, *B*, and *C* are 50-Ω TEM transmission lines, while region *D* is a standard rectangular waveguide. In each case, the × shows the approximate beam position within the cross section. Also shown, for each region, are its operating frequency range and the maximum value of the reflection coefficient from one end of the region.

electrons. To a sufficient approximation, these can be written as [11]:

$$H_{\mathrm{spin}}=[b\vec{I}\cdot\vec{S}_c+c(\vec{I}\cdot\hat{\boldsymbol{\rho}})(\hat{\boldsymbol{\rho}}\cdot\vec{S}_c)+d\vec{R}\cdot\vec{S}_c] + \frac{\alpha^2\mathrm{Ry}}{r^3}\{\vec{L}\cdot\vec{S}_R-2\vec{L}\cdot\vec{S}_c+2\vec{S}_R\cdot[\vec{S}_c-3\hat{\mathbf{r}}(\hat{\mathbf{r}}\cdot\vec{S}_c)]\} - V_x(\tfrac{1}{2}+2\vec{S}_c\cdot\vec{S}_R), \quad (3)$$

where b, c, and d are hyperfine constants of the free ion, I is the total nuclear spin, and S_c, S_R are the spins of the core and Rydberg electron. V_x is the exchange energy, which is negligible for all but the lowest-L states ($L=4$) studied here. Since the effect of the interactions in H_{spin} is only to produce the substructure on the rf resonances, we will assume theoretical values of the hyperfine constants [12] to calculate the structure.

Using these constants, H_{spin} can be diagonalized within the $(0,0)nL$ space. The results are illustrated in Fig. 5, which shows the spin structure of a typical level $(0,0)10H_5$ of both H_2 and D_2. In the case of H_2, the spin structure is very simple. Since $I=0$ for an $R=0$ state of H_2^+, there is no hyperfine structure, and the only spin structure results from the magnetic and exchange interactions in H_{spin}. These are exactly the same as the interactions that occur in Rydberg

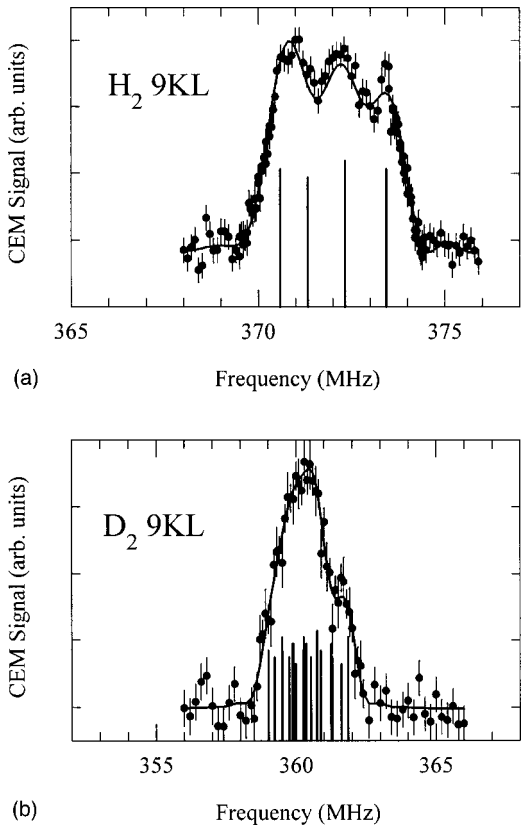

FIG. 4. Typical examples of rf resonance signals observed for (a) H_2 and (b) D_2. Both signals correspond to the $9K$-$9L$ transition for rf and molecular beam copropagating. The smooth curves correspond to fits of the signals to the theoretical composite line shape described in the text. The stick diagram shows the positions of the individual resonance components.

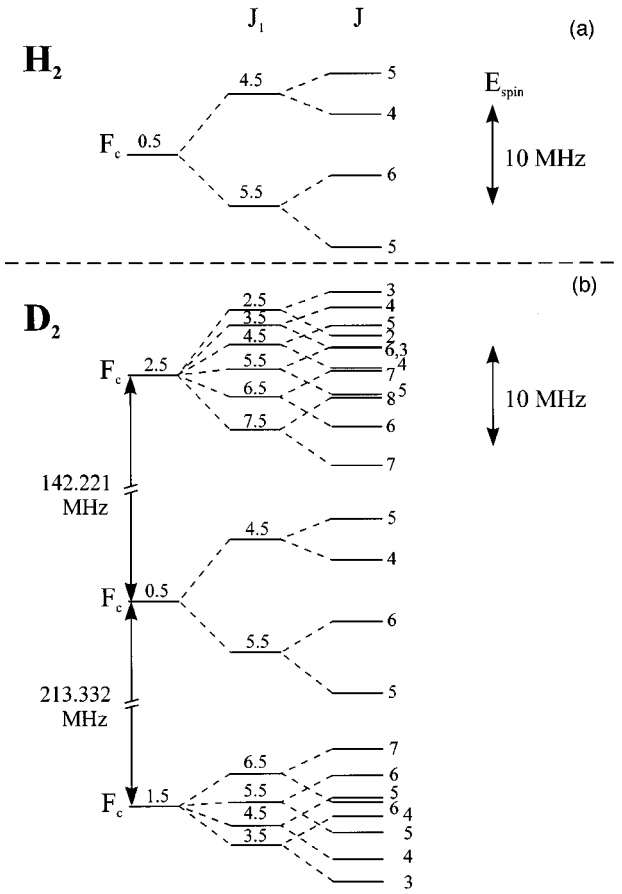

FIG. 5. Calculated spin structure for the $(0,0)10H_5$ state of (a) H_2 and (b) D_2. In the case of H_2, only four sublevels exist, just as in the helium atom. In D_2, however, there are 24 separate spin-structure levels, as described in the text. This spin structure leads to the 4- and 24-component stick diagrams in Fig. 4.

states of the helium atom [13] and result in the same fourfold splitting of the $(0,0)nL$ state. This structure is almost entirely due to the two spin-orbit terms in $H_{\rm spin}$. One possible difference between the spin structure of H_2 and He is the size of the exchange energy V_x, which would be expected to be larger for H_2 since the H_2^+ core is larger than the He^+ core. Indeed, fitting the positions of the four well-resolved spin components of the $10G$-$10H$ transition in H_2 leads to the conclusion that $V_x(10G)=1.12(20)$ MHz. This is still much smaller than the spin-orbit magnetic structure, so the total electron spin quantum number is spoiled just as in the helium atom. The same value is assumed for the exchange energy in D_2, while V_x is taken to be zero for all levels with $L>4$.

In the case of D_2, the structure is more complicated. Here $I=0$ or 2 for the $R=0$ state, and so there are three possible values of the total core spin:

$$\vec{F}_c=\vec{I}+\vec{S}_c.$$

The hyperfine splittings between these three levels are relatively large, even larger than many of the fine-structure intervals to be measured. However, electric dipole selection rules forbid transitions between states of different F_c, so these intervals do not contribute to the observed resonance substructure. When F_c is coupled to N and S_R, however, 24 eigenstates result, as illustrated for one case in Fig. 5. Electric dipole selection rules strongly favor transitions between corresponding eigenstates in adjacent L manifolds, so this results in 24 closely spaced transition frequencies instead of the four seen in H_2. The smooth curves in Fig. 4 are fits of observed resonances to a superposition of four (H_2) or $24\,(D_2)$ spin components. The component positions relative to the ''spinless'' transition frequency are taken from these calculations, and their relative strengths are taken to be proportional to the statistical weight of the lower-L state of the transition. The value of the ''spinless'' interval that is extracted from these fits is what we report here as the fine-structure interval. We consider later the uncertainty introduced into the measurement by this unresolved substructure.

For each fine-structure interval, measurements were taken for both directions of propagation of the rf field with respect to the beam velocity. Table I shows the fitted center frequencies for both Doppler shift directions and their geometric mean, which is our best estimate of the transition frequency for stationary molecules [14]. The uncertainties shown there are entirely statistical, resulting from the fit.

In order to estimate the additional uncertainty in the spinless fine-structure interval due to the effects of the unresolved spin structure, we used the $10G$-$10H$ and $10H$-$10I$

TABLE I. Fitted values of the H_2 and D_2 fine-structure intervals. The errors shown for ν_+, ν_-, and ν_0 are purely statistical errors. The rf regions used for each measurement are identified in the notation of Fig. 3.

Interval	rf region	ν_+ (MHz)	ν_- (MHz)	ν_0 (MHz)
		H_2		
10*G*-10*H*	*D*	5188.044(34)	5159.867(37)	5173.936(25)
10*H*-10*I*	*A*	1664.896(11)	1653.544(9)	1659.210(7)
10*I*-10*K*	*A*	632.945(8)	628.649(7)	630.793(5)
10*K*-10*L*	*A*	274.982(18)	273.167(19)	274.073(13)
10*L*-10*M*	*A*	130.073(15)	129.275(13)	129.673(10)
10*L*-10*M*	*A*(reversed)	130.128(15)	129.219(12)	129.673(10)
9*H*-9*I*	*C*	2311.11(33)	2296.29(33)	2303.69(23)
9*I*-9*K*	*A*	867.518(6)	861.621(6)	864.564(4)
9*K*-9*L*	*A*	371.962(9)	369.431(6)	370.694(5)
		D_2		
10*G*-10*H*	*D*	5334.08(11)	5316.82(10)	5325.44(7)
10*H*-10*I*	*B*	1691.45(9)	1683.42(8)	1687.43(6)
10*I*-10*K*	*A*	639.576(8)	636.507(11)	638.040(7)
10*K*-10*L*	*A*	273.698(11)	272.392(11)	273.044(8)
10*L*-10*M*	*A*	129.741(10)	129.132(9)	129.436(7)
9*I*-9*K*	*B*	875.389(45)	871.139(33)	873.261(28)
9*K*-9*L*	*A*	360.390(17)	358.646(19)	359.517(13)

resonances in H_2, which show well-resolved spin structure, to check the validity of the assumptions used in fitting the other resonances. When these resonances were fitted, freely varying the amplitude and position of each of the four components, they indicated that the relative positions of the four components were correct to within about 0.1% of the predicted spin structure. In addition, the fitted relative amplitudes agreed with the assumed statistical weights to within about 10%. When we simulated compound resonances with this degree of variation in amplitudes, and fitted these to our assumed form, the fitted center was altered by about 1% of the unresolved linewidth. For example, in Fig. 4, which shows the 9*K*-9*L* resonances for H_2 and D_2, we estimated the unresolved width as 3.5 MHz. We assigned an additional uncertainty equal to 1% of this unresolved width to reflect our uncertainty in the precise underlying structure in the rf resonances. In the two cases where the spin structure was fully resolved, 10*G*-10*H* and 10*H*-10*I* in H_2, we assigned an additional uncertainty equal to 0.1% of the largest spin displacement. These uncertainties, σ_{spin}, are shown in Table II, along with other systematic uncertainties. For comparison, the purely statistical uncertainties for the line fits, σ_{fit}, are also shown in Table II. For all except the fully resolved cases, σ_{spin} dominates over σ_{fit} indicating that the primary limit in the precision of this measurement is the unresolved spin structure.

Another potentially important systematic effect is the possible presence of stray electric fields, which could Stark-shift the observed resonances from their true positions. Such stray fields, in the range 0–100 mV/cm, have proved to be a persistent difficulty in similar studies of atomic helium fine structure [6]. They are a much less severe problem here since the larger fine structure of H_2 and D_2 is less sensitive to stray fields. In order to reduce stray fields due to motional fields, all four rf interaction regions were enclosed in mu-metal shielding to reduce the earth's magnetic field to less than 20 mG. In this experiment, the ambient stray electric fields were measured by using high-*n* rf transitions in helium as stray-field meters. These transitions shift rapidly in electric fields, and their zero-field positions have been calculated precisely enough [15] that they can be considered to be known exactly. Table III lists six transitions in helium that were used for the

TABLE II. Uncertainties and systematic corrections for each measured interval. All results are in kHz. The values for σ_{ref} and ΔE_{stark} are shown to 0.1 kHz precision for clarity, while the net result is rounded to the nearest kHz.

Interval	σ_{fit}	σ_{spin}	σ_{ref}	$-\Delta E_{\text{stark}}$	Cor$\pm\sigma_{\text{tot}}$
			H_2		
10*G*-10*H*	±25	±10	±0.3	+1.3±0.4	1±27
10*H*-10*I*	±7	±6	±0.6	0.1±0.1	0±9
10*I*-10*K*	±5	±20	±1.5	0.0±0.0	0±21
10*K*-10*L*	±13	±20	±3.8	−0.1±0.1	0±25
10*L*-10*M*	±7	±20	±0	−0.4±0.1	0±21
9*H*-9*I*	±230	±100	±14.0	+0.5±0.2	0±251
9*I*-9*K*	±4	±11	±1.1	−0.1±0.1	0±12
9*K*-9*L*	±5	±30	±2.6	−0.8±0.2	−1±30
			D_2		
10*G*-10*H*	±70	±110	±0.2	+1.4±0.4	1±130
10*H*-10*I*	±60	±70	±0.9	+15.0±5.0	15±92
10*I*-10*K*	±7	±40	±1.1	0.0±0.0	0±41
10*K*-10*L*	±8	±30	±2.5	−0.2±0.1	0±31
10*L*-10*M*	±7	±20	±7.9	−0.6±0.2	−1±22
9*I*-9*K*	±28	±60	±1.8	−1.9±0.6	−2±66
9*K*-9*L*	±13	±35	±1.9	−0.3±0.1	0±37

TABLE III. Stray electric field diagnostic lines.

Label	Transition	ν_0 (MHz)	Shift rate [MHz/(V/Cm)^2]
	Primary		
1	He: 27 $^1F_3$-27$^1G_4$	105.065	−7904
2	He: 27 $^1D_2$-27$^1F_3$	558.643	−1882
3	He: 27 $^3F_3$-27$^3G_4$	106.493	−7602
4	He: 17 $^3F_3$-17$^3G_4$	424.049	−281.3
5	He: 27 $^1P_1$-27$^1D_2$	4757.09	+1059.7
6	He: 10 $^3G_5$-10$^3H_6$	491.967	−11.62
	Secondary		
7	H_2: (0,1)27H_6-(0,1)27I_7	196.800(22)	−956.2
8	D_2: (0,2)27I_3-(0,2)27K_9	112.699(6)	−945.3

primary diagnostic transitions in this work, showing their zero-field position and Stark-shift rate. Using these primary diagnostics, two secondary transitions, in H_2 and D_2, were calibrated, i.e., their zero-field positions were determined by Stark-shift corrections derived from one of the primary diagnostic lines. These secondary diagnostics were more convenient to use since they did not require a change of ion beams. Once the rms stray electric field was determined from one of these diagnostic lines, the Stark shift of the resonance under study could be calculated and a correction could be applied to the measured line center. The Stark-shift rates of each of the measured resonances range from 0.3 to 11.0 MHz/(V/cm^2). The inferred Stark-shift corrections for each of the transitions, shown in Tables II and IV, are generally very small.

Another potential systematic error comes from the fact that the rf electric field encountered in the rf interaction region is not a completely pure traveling wave (either with or against the Rydberg beam), but contains a small component of oppositely traveling wave due to reflections at the output end of the rf region. When the reflection coefficient Γ is small, its primary effect on the resonance line shape is through interference with the larger traveling wave, leading to a line shape of the form

$$S(\nu)=\left(\frac{\sin[\pi(\nu_+-\nu)T]}{[\pi(\nu_+-\nu)T]}\right)^2+2\,\mathrm{Re}(\Gamma)\times\left(\frac{\sin[\pi(\nu_+-\nu)T]}{[\pi(\nu_+-\nu)T]}\,\frac{\sin[\pi(\nu_--\nu)T]}{[\pi(\nu_--\nu)T]}\right) \quad (4)$$

where

$$\nu_+=\nu_0\left(\frac{\sqrt{1+v/c}}{\sqrt{1-v/c}}\right) \quad \text{and} \quad \nu_-=\nu_0\left(\frac{\sqrt{1-v/c}}{\sqrt{1+v/c}}\right).$$

The second term, proportional to Re(Γ), can shift the center of the first term by an amount that depends on Γ, β, ν_0, and T. The reflection coefficient Γ is the reflection from the output end of the rf region. If, when the direction of rf propagation is reversed, the reflection coefficient of the other physical end of the region is identical in amplitude and phase, then the two line-center shifts cancel exactly. In previous studies [6], the physical ends of the rf region were routinely reversed to ensure that on the average the two ends would be identical. In this study, estimation of the typical reflection coefficients of the rf regions (see Fig. 3) showed that this was not necessary in most cases. Even assuming that the reflection coefficients from the two ends differed by a factor of 2 (a very cautious estimate in view of measurements of the net reflection from both ends) leads to a possible line-center shift that is small compared to statistical errors. These calculated possible line shifts are taken to represent a one standard deviation uncertainty from this effect, and are shown in Table II as σ_{ref}. In the one case that was closest to being significant, the 10L-10M interval, this estimate indicated a possible shift of 14 kHz. As a check, we implemented the physical reversal of the rf region A for this one interval, and found a difference of 0(14) kHz between the results measured with the two different orientations of

TABLE IV. Measured Stark shifts of H_2 and D_2 transitions at average ambient stray electric fields, as determined using the diagnostics of Table III.

Interval	Diagnostic no.	E_{stray} (mV/cm)	Shift rate [MHz/(v/cm)^2]	$\Delta E_{\mathrm{stark}}$ (MHz)
		H_2		
10G-10H	5	36.5	−1.01	−0.0013
10H-10I	7	6.9	−1.98	−0.0001
10I-10K	7	6.5	−0.36	0.0000
10K-10L	3	8.4	+2.05	+0.0001
10L-10M	3	7.6	+10.75	+0.0006
10L-10M	1	4.6	+10.75	+0.0002
9H-9I	2	34.1	−0.39	−0.0005
9I-9K	4	15.7	+0.35	+0.0001
9K-9L	4	15.9	+2.98	+0.0008
		D_2		
10G-10H	5	36.5	−1.03	−0.0014
10H-10I	6	86.5	−2.01	−0.0150
10I-10K	8	8.6	−0.37	0.0000
10K-10L	8	8.8	+2.08	+0.0002
10L-10M	8	7.2	+10.93	+0.0006
9I-9K	6	71.9	+0.36	+0.0019
9K-9L	8	9.6	+3.03	+0.0003

the rf region, as shown in Table I. By directly averaging the results obtained for the two orientations of the rf region, this uncertainty was completely eliminated for the H_2 $10L$-$10M$ interval.

III. DATA ANALYSIS AND RESULTS

A direct comparison between measured intervals and theoretical predictions is clouded by the fact that the coefficient of the leading term in the theory, α_S, has not been calculated at the level of precision of the measurements. Consequently, we will instead use the measurements to determine a value of α_S. This analysis is based on the assumption that each measured interval can be expressed as

$$\Delta E = \Delta E^{[1]} + \Delta E^{[2]} + \Delta E^{[3]} + \Delta E^{\mathrm{rel}}, \tag{5}$$

where $E^{[i]}$ represents the ith order perturbation energy in V_{eff} and E^{rel} is the relativistic correction to the kinetic energy. The first term, $\Delta E^{[1]}$, is almost entirely responsible for the observed fine-structure intervals, with the last three terms giving only small corrections. We will calculate each of the last three terms and subtract their contributions from the measured value of each interval. This will give an experimental estimate of $\Delta E^{[1]}$, from which α_S may be determined. Both $E^{[2]}$ and $E^{[3]}$ contain, in principle, many different multipole contributions from the various terms in V_{eff}. Both expressions simplify considerably when applied to a state with $R=0$, as is the case here. For example, each tensor order in V_{eff} couples to a unique value of R' in $E^{[2]}$, leading to the expression (in atomic units)

$$\begin{aligned} E^{[2]}((0,0)nL_L) &= \sum_{\nu',n'} \frac{|\langle (0,0)nL_L|[\alpha_S(\rho)/2](1/r^4)+[C_0/10-3\beta_S(\rho)/2](1/r^6)|(\nu',0)n'L_L\rangle|^2}{E(0,0,n)-E(\nu',0,n')} \\ &+ \sum_{\nu',n'L'} \frac{|\langle (0,0)nL_L|\{Q(\rho)(1/r^3)+\alpha_T(\rho)/3(1/r^4)+[C_1(\rho)/7-\beta_T(\rho)/2+E_1(\rho)/7](1/r^6)\}P_2(\cos\theta)|(\nu',2)n'L'L\rangle|^2}{E(0,0,n)-E(\nu',2,n')}. \end{aligned} \tag{6}$$

A similar expression involving the fourth-order tensors, proportional to $P_4(\cos\theta)$, has been omitted for reasons that will be explained shortly. Each of the terms shown could be sorted according to matrix element products proportional to a given total inverse power of r, r^{-s}. The first term contains three products with $s=8$, 10, and 12, while the second contains $s=6$, 7, 8, 9, 10, and 12. We find that the contribution of these separate products decreases with s, and so choose to truncate the expression after terms up to $s=9$ have been included. The omitted sum from fourth-order tensors contains no terms of this order. In addition, we the limit sum over ν' to $\nu'=0,1,2$ only, since the contributions of higher vibrational levels also decrease rapidly. In order to illustrate these truncations, Table V shows the calculated contributions to a typical level $(0,0)10H_5$ separated according to s and ν'.

In our previous report [5] values of $E^{[2]}$ were calculated by an explicit summation over discrete levels n' and numerical integration over the continuum states. For this report, we have recalculated all the $E^{[2]}$'s using the Dalgarno-Lewis method [16], in which the summation is replaced by the solution of a differential equation. This reduces the numerical uncertainty in the result, and also increases confidence in the mutually consistent results. The remaining uncertainty in the calculated $E^{[2]}$'s comes from the parameters that enter the calculation, namely, the values of the matrix elements of the various core properties between different rovibrational states of the core and also the energies of the various rovibrational states themselves. Since, as Table V illustrates, the net result is dominated by the $s=6$, $\nu'=0$ contribution, the most critical parameters are the matrix element of $Q(\rho)$ between the (0,0) and (0,2) core levels and the energy difference between these two core levels. The matrix elements used,

$$\langle 0,0|Q(\rho)|0,2\rangle = \begin{cases} 1.644\,55 e a_0^2 & \text{for } H_2^+ \\ 1.608\,62 e a_0^2 & \text{for } D_2^+, \end{cases}$$

were calculated using the adiabatic wave functions for the core ions [17], and are expected to be accurate at the level of 0.2%. This leads to a 0.4% uncertainty in the calculated $E^{[2]}$'s.

The other critical core property is the excitation energy between the (0, 0) and (0, 2) core states. Here we have used values from the literature [18,19],

TABLE V. Contributions to $E^{[2]}((0,0)10H_5)$, sorted by s and ν'. This illustrates the convergence by which the calculation's truncation is justified. The total value for this state is 47.41(190) MHz.

s	$\nu'=0$	$\nu'=1$	$\nu'=2$
6	47.405	−0.797	0.028
7	3.463	0.002	−0.007
8	−2.350	−0.323	0.000
9	−0.006	0.000	0.000

TABLE VI. Calculated values of $\Delta E^{[2]}$, $\Delta E^{[3]}$, and ΔE^{rel} for each measured transition. Tabulated uncertainties for $\Delta E^{[2]}$ *do not* include the 0.2% uncertainty in the $\langle 00|Q|02\rangle$ matrix element, but do include the estimated convergence error and the 0.2% uncertainty in all other matrix elements. Uncertainties for $\Delta E^{[3]}$ are estimated at about 10%. The final column shows the total of these calculated contributions to each measured interval.

Transition	$\Delta E^{[2]}$ (MHz)	$\Delta E^{[3]}$ (MHz)	ΔE^{rel} (MHz)	ΔE^{calc} (MHz)
		H_2		
(0,0)10*G*-*H*	−110.521(105)	+0.654(65)	+7.076	−102.791(123)
(0,0)10*H*-*I*	−32.822(5)	−0.030(3)	+4.899	−27.953(6)
(0.0)10*I*-*K*	−12.056(7)	−0.028(3)	+3.593	−8.491(8)
(0,0)10*K*-*L*	−2.555(3)	+0.002(0)	+2.747	+0.194(3)
(0,0)10*L*-*M*	−1.082(0)	−0.002(0)	+2.169	+1.085(0)
(0,0)9*H*-*I*	+22.091(26)	−0.044(4)	+6.720	+28.767(26)
(0,0)9*I*-*K*	+4.116(7)	−0.025(3)	4.928	+9.019(8)
(0,0)9*K*-*L*	+3.784(4)	−0.008(1)	+3.769	+7.545(4)
		D_2		
(0,0)10*G*-*H*	+194.795(178)	+0.242(24)	+7.077	+202.114(180)
(0,0)10*H*-*I*	+45.281(25)	−0.159(16)	+4.900	+50.022(30)
(0,0)10*I*-*K*	+14.222(5)	−0.045(5)	+3.593	+17.770(7)
(0,0)10*K*-*L*	+4.580(2)	−0.013(1)	+2.747	+7.314(2)
(0,0)10*L*-*M*	+2.521(1)	−0.004(1)	+2.170	+4.687(2)
(0,0)9*I*-*K*	+38.416(33)	−0.235(24)	+4.929	+43.110(47)
(0,0)9*K*-*L*	+3.044(35)	+0.353(35)	+3.769	+7.166(49)

$$E(0,2)-E(0,0)=\begin{cases}174.238\ \mathrm{cm}^{-1} & \text{for } H_2{}^+\\ 88.050\ \mathrm{cm}^{-1} & \text{for } D_2{}^+.\end{cases}$$

These values are probably accurate to better than 0.010 cm^{-1}. In the one case where similar values have been tested by a precise experiment, the (0, 1)-(0, 3) rotational interval in $H_2{}^+$ was confirmed to an accuracy of 0.002 cm^{-1} [3]. Even if we assume an uncertainty of 0.010 cm^{-1}, however, the resulting uncertainty in the calculated $E^{[2]}$'s is negligible in comparison with the uncertainty from the quadrupole matrix element.

Another type of uncertainty in the calculated $E^{[2]}$'s arises from the truncation of the multipole series. In our previous report [5], where only terms up to $s=8$ were included in the calculation, this was the dominant source of error. By including the $s=9$ terms here, however, the uncertainty due to the truncation, which we estimate by half the smallest term, is greatly reduced. The total calculated values of $\Delta E^{[2]}$ for all the transitions involved in this study are shown in Table VI. The uncertainty shown there does not include the 0.4% uncertainty in the leading term ($s=6$, $\nu=0$), but does include a 0.4% uncertainty in all other contributions and also the truncation error.

In view of the improved precision of $E^{[2]}$, we were concerned that $E^{[3]}$ might contribute at a level comparable to the uncertainty in $E^{[2]}$. With this in mind, we calculated the leading terms in $E^{[3]}$, which have $s=9$ and 10, and result from the expression

$$E^{[3]}((0,0)nL_L)=\sum_{\substack{\nu',R',n',L'\\ \nu'',R'',n'',L''}}\frac{\langle(0,0)nL_L|V|(\nu',R')n'L'_L\rangle\langle(\nu',R')n'L'_L|V|(\nu'',R'')n''L''_L\rangle\langle(\nu'',R'')n''L''_L|V|(0,0)nL_L\rangle}{[E(0,0,n)-E(\nu',R',n')][E(0,0,n)-E(\nu'',R'',n'')]}$$

$$-\langle(0,0)nL_L|V|(0,0)nL_L\rangle\sum_{\nu',R',n',L'}\frac{\langle(0,0)nL_L|V|(\nu',R')n'L'_L\rangle\langle(\nu',R')n'L'_L|V|(0,0)nL_L\rangle}{[E(0,0,n)-E(\nu',R',n')]^2},\qquad(7)$$

where, for present purposes,

$$V=V_Q+V_{\alpha_T}+V_{\alpha_S}$$

where each term represents the part of V_{eff} proportional to Q, α_T, and α_S.

As in the case of $E^{[2]}$, the sums over n' and n'' can be

TABLE VII. Values of $\Delta E^{[1]}$, inferred from measurements and calculated higher-order terms. Column 3 shows the values inferred from this study, while column 2 shows the less precise values reported previously. Column 4 shows the values returned with the best-it values of the parameters B_4, B_6, B_7, and B_Q, as described in the text.

Interval	$\Delta E^{[1]}$ [5]	$\Delta E^{[1]}$ (this work)	$\Delta E^{[1]}$ (fit)
		H_2	
10*G*-10*H*		5276.728(126)	5276.731
10*H*-10*I*	1687.4(1.4)	1687.163(11)	1687.162
10*I*-10*K*	639.31(18)	639.284(22)	639.297
10*K*-10*L*	273.83(4)	273.879(25)	273.854
10*L*-10*M*		128.588(21)	128.599
9*H*-9*I*		2274.923(252)	2274.982
9*I*-9*K*	855.49(22)	855.545(14)	855.550
9*K*-9*L*	363.12(4)	363.148(30)	363.106
		D_2	
10*G*-10*H*		5123.327(222)	5123.330
10*H*-10*I*	1637.8(1.3)	1637.423(97)	1637.396
10*I*-10*K*	620.19(17)	620.270(42)	620.298
10*K*-10*L*	265.76(8)	265.730(31)	265.698
10*L*-10*M*		124.748(22)	124.763
9*I*-9*K*	830.25(22)	830.149(78)	830.175
9*K*-9*L*	352.25(8)	352.351(61)	352.309

replaced by solutions of a differential equation, and this reduces the expression to a simple radial integral for each choice of operators and of ν', L', ν'', L''. The result does indeed turn out to be comparable to the quoted uncertainty in $E^{[2]}$, and therefore not negligible. The uncertainty in $E^{[3]}$ is taken to be 10% of the result, since terms with $s=11$ have not been calculated. The calculated values of $\Delta E^{[3]}$ for all the transitions of this study are also shown in Table VI.

The relativistic corrections to the fine-structure intervals are due to the p^4 term in the kinetic energy, and have been given elsewhere [1]. The appropriate corrections for the finite mass of the ions have been discussed recently [20]. Table VI shows the calculated contribution of ΔE^{rel} for the transitions of this study. The sum of these three contributions represents the total calculated contribution to each transition, and is also shown in Table VI.

Using the values of $\Delta E^{[2]}$, $\Delta E^{[3]}$, and ΔE^{rel} from Table VI, the measured fine-structure intervals from Table I, corrected as indicated in Table II, can be used to infer experimental estimates of $\Delta E^{[1]}$. The results are shown in Table VII, along with the estimates reported previously [5]. The uncertainties quoted for the new estimates of $\Delta E^{[1]}$ include only the statistical errors from Table I and the errors in ΔE^{calc} from Table VI, but of course still exclude the uncertainty due to the $\langle 00|Q|02\rangle$ matrix element.

In order to extract the best values of α_S, we fit all the data to the form

$$\Delta E^{[1]} = B_4 \Delta\langle r^{-4}\rangle + B_6 \Delta\langle r^{-6}\rangle + B_7 \Delta\langle r^{-7}\rangle,$$

where the radial expectation values are standard functions of n and L, with appropriate reduced mass corrections, and all terms are expressed in a.u. In this fit, the coefficients B_4, B_6, and B_7 vary freely for each ion. Only the errors shown in Table VII are considered in the fit. The resulting fit matches the data to within these statistical errors for the D_2 measurements ($\chi^2=2.8$ for four degrees of freedom) and very nearly so for the H_2 measurements ($\chi^2=16.4$ for five degrees of freedom). Examination of the fit residuals, however, shows that they are not random, but can be significantly reduced by a small adjustment in the size of the leading contribution to $\Delta E^{[2]}$. This, of course, would be the effect of adjusting the size of the $\langle 0,0|Q|0,2\rangle$ matrix element. Since the degree of adjustment required for the best fit of the data is comparable to our estimated uncertainty in these matrix elements, we choose to let the fit determine the best values. This is equivalent to expanding the fit of the $\Delta E^{[1]}$ values shown in Table VII to include an additional term:

$$\Delta E^{[1]} = B_4 \Delta\langle r^{-4}\rangle + B_6 \Delta\langle r^{-6}\rangle + B_7 \Delta\langle r^{-7}\rangle - B_Q \Delta E^{[2]}(s=6,\ \nu'=0).$$

TABLE VIII. Best-fit parameters resulting from fits of $\Delta E^{[1]}$.

	H_2	D_2
B_4	−1.583 98(7)	−1.535 93(27)
B_6	7.877(43)	7.421(86)
B_7	−18.80(27)	−17.48(58)
B_Q	0.0052(14)	0.0029(59)
χ^2	3.84	2.60
Degrees of freedom	4	3

This expanded fit gives an excellent fit of all the data for both isotopes. The fitted values of $\Delta E^{[1]}$ are shown for comparison in Table VII, and the best-fit parameters are summarized in Table VIII. The rms relative deviation of the fitted $\Delta E^{[1]}$'s is less than 0.01% for both isotopes, as illustrated in Table VII.

The fitted values of B_Q indicate that the adiabatic calculations of the $\langle 0,0|Q|0,2\rangle$ matrix element [17] overestimate the matrix element by 0.26(7)% in H_2^+ and 0.15(30)% in D_2^+. Although nonadiabatic calculations of these matrix elements have not yet been reported, the required correction to the adiabatic matrix element in H_2^+ is only about a factor of 2 larger than the correction reported for the $\langle 00|\alpha_s|00\rangle$ matrix element [21]. The fitted coefficients B_6 are in reasonable agreement with those calculated recently by Taylor, Dalgarno, and Babb ($H_2$7.77,$D_2$7.24) [21]. The coefficients B_4 give our best estimates of the ion polarizabilities:

$$\alpha_S(H_2^+(0,0)) = 3.167\,96(15)\,a_0^3;$$

$$\alpha_s(D_2^+(0,0)) = 3.071\,87(54)\,a_0^3.$$

TABLE IX. Comparison between measured and calculated values of ground-state scalar polarizabilities of H_2^+ and D_2^+. All results in units of a_0^3.

	$\alpha_S(H_2^+(0,0))$	$\alpha_S(D_2^+(0,0))$
Experiment		
Jacobson *et al.* [5]	3.168 1(7)	3.071 2(7)
This report	3.167 96(15)	3.071 87(54)
Theory (adiabatic)		
Jacobson *et al.* [5]	3.173 0	3.073 9
Theory (nonadiabatic)		
Bhatia and Drachman [27]	3.168 0	3.067 1
Shertzer and Greene [28]	3.168 2(4)	3.071 4(4)
Taylor and Babb [21]	3.168 725 6(1)	3.071 988 7(2)
Moss [29]	3.168 726	3.071 989

The smaller uncertainty for the H_2^+ result is due to a combination of factors. First, the statistical errors are smaller for H_2^+ due to better S/N ratio and simpler spin structure. Secondly, the pattern of measurements gives tighter determination of the $\langle 00|Q|02\rangle$ matrix element for H_2^+ because of the change in sign of $\Delta E^{[2]}(s=6, v'=0)$ between the $n=9$ and 10 intervals for that isotope.

In relating B_4 and α_S, we use the simple correspondence

$$B_4 = \frac{-\alpha_s}{2}$$

instead of the equation used in our earlier report,

$$B_4 = (1+\varepsilon)^2 \frac{(-\alpha_s)}{2} \quad \text{where} \quad \varepsilon \equiv \frac{m_e}{2M_N + m_e}.$$

We had argued [22] that the factor $(1+\epsilon)^2$, which occurs in the derivation of the polarization potential, should not be included in the definition of α_S, and that therefore the coefficient B_4 should be written with this factor shown explicitly. However, in the meantime, several sources have pointed out that precisely this factor occurs in any derivation of the energy shift of the H_2^+ ion in an electric field, and so it is naturally included in the definition of α_S [23].

Table IX compares the measured values of the polarizabilities with theory. Prior to our initial report [5], the only existing calculations used the adiabatic approximation, which is likely to be in error at the level of m_e/M_N, about 0.1% for H_2^+. The initial report was sufficiently precise to indicate the need for improved calculations. This is illustrated for the case of H_2^+ in Fig. 6. Since that time, a number of new calculations have appeared that do not make the adiabatic approximation. The results of these ''nonadiabatic'' calculations are summarized in Table IX. The most precise of these new calculations, that of Taylor, Dalgarno, and Babb [21], is also illustrated in Fig. 6. The value of α_s reported here for H_2^+ is sufficiently precise to reveal a clear discrepancy with this calculation. The less precise result reported for D_2^+ is in satisfactory agreement with the same

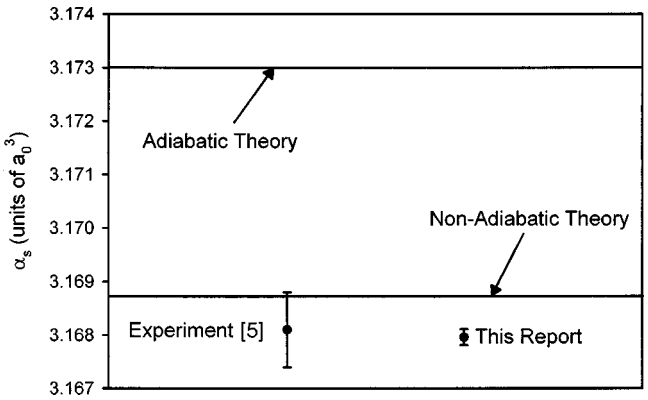

FIG. 6. Comparison of calculated and measured values of the polarizability of $H_2^+(0,0)$. The horizontal lines show the adiabatic and more recent nonadiabatic calculations, as shown in Table IX. The points show the result of the preliminary [5] and present versions of this experiment.

calculation. Specifically, the comparison between our measurements and the calculation of Ref. [21] gives

$$\frac{\alpha_s(H_2^+)}{T_{\rm NA}} = 1 - 0.000\,242(47),$$

$$\frac{\alpha_S(D_2^+)}{T_{\rm NA}} = 1 - 0.000\,039(176).$$

There are a number of effects, so far omitted from all the calculations, that could possibly affect the result at this level. Among these are relativistic, radiative, and retardation corrections. However, if the nonadiabatic calculation has eliminated discrepancies of relative order m_e/M_N, then one would expect each of these omitted terms to contribute approximately equally to both isotopes. This is not ruled out by the experimental results, which are consistent with their weighted average,

$$\left(\frac{\alpha_S}{T_{\rm NA}}\right)_{\rm Isotope\ \ average} = 1 - 0.000\,228(45).$$

Perhaps by coincidence, this is about the level at which these omitted terms enter into calculations of the polarizability of the He^+ ion. In that case, the nonrelativistic result can be calculated analytically, and is equal to $\frac{9}{32}$ [24]. Relativistic corrections reduce this by 0.022% [25]. There are additional corrections to the energy of helium Rydberg states due to retardation and radiative corrections which are proportional to $\langle r^{-4}\rangle$ and which are therefore effectively corrections to the polarizability [26]. The retardation corrections are equivalent to a further reduction of 0.010%, while the radiative corrections lead to an increase of +0.003%. While there may be semantic questions as to which of these ought to be included in the definition of the H_2^+ polarizability, all of them would clearly be included in the experimental result quoted above. Further theoretical study will be required to estimate the size of these additional corrections for H_2^+ and

D_2^+. They may well account for the discrepancy between this measurement and the most recent theoretical predictions.

For the present, we conclude that the measured polarizabilities agree with *a priori* nonadiabatic calculations at the level of 0.02%, but the experiment, especially the H_2 result, indicates additional contributions at about this level. Clear confirmation of any such additional contributions would require improved measurements. Some significant improvement with the present technique should be possible by (a) improved treatment of the unresolved spin structure, and (b) widening the data pattern to include $n=11$ states as a further check on the critical $E^{[2]}$ contributions. The $n=11$ measurements would be especially helpful in the case of D_2, where the weak variation in $\Delta E^{[2]}(s=6, v'=0)$ between $n=9$ and 10 is an important limitation on the present measurement.

ACKNOWLEDGMENTS

We acknowledge the assistance of Daniel Fisher and Charles Fehrenbach in constructing portions of the apparatus used for these measurements. This work was supported by the National Science Foundation through Grant No. PHY97-31618.

[1] W. G. Sturrus, E. A. Hessels, P. W. Arcuni, and S. R. Lundeen, Phys. Rev. A **44**, 3032 (1991).
[2] Z. W. Fu, E. A. Hessels, and S. R. Lundeen, Phys. Rev. A **46**, R5313 (1993).
[3] P. W. Arcuni, Z. W. Fu, and S. R. Lundeen, Phys. Rev. A **42**, R6950 (1990).
[4] For a recent review of both measurements and calculations relating to the H_2^+ system, see Christine A. Leach and Richard E. Moss, Annu. Rev. Phys. Chem. **46**, 55 (1995).
[5] P. L. Jacobson *et al.* Phys. Rev. A **56**, R4361 (1998); **57**, 4065(E) (1998).
[6] G. D. Stevens and S. R. Lundeen, Phys. Rev. A **60**, 4379 (1999).
[7] R. W. Dunford, Ph.D. dissertation, University of Michigan, 1978 (unpublished).
[8] T. J. Morgan, C. F. Barnett, J. A. Ray, and A. Russek, Phys. Rev. A **20**, 1062 (1979).
[9] W. G. Sturrus, P. E. Sobol, and S. R. Lundeen, Phys. Rev. Lett. **54**, 792 (1985).
[10] F. von Busch and G. H. Dunn, Phys. Rev. A **5**, 1726 (1972).
[11] W. G. Sturrus, E. A. Hessels, and S. R. Lundeen, Phys. Rev. Lett. **57**, 1863 (1986).
[12] J. F. Babb (private communication): $H_2^+(0,0)$: $b=881.547$, $c=128.731$, $d=42.526$; $D_2^+(0,0)$: $b=135.885$, $c=19.99$, $d=21.52$. All results in MHz.
[13] E. A. Hessels, W. G. Sturrus, and S. R. Lundeen, Phys. Rev. A **35**, 4489 (1987).
[14] This is not quite correct for the transitions using the waveguide region (D), but the corrections are insignificant compared with experimental errors.
[15] G. W. F. Drake, Adv. At., Mol., Opt. Phys. **32**, 93 (1994).
[16] R. A. Komara, W. G. Sturrus, D. H. Pollack, and W. R. Cochran, Phys. Rev. A **59**, 251 (1999).
[17] J. F. Babb (private communication).
[18] G. Hunter, A. W. Yau, and H. O. Pritchard, At. Data Nucl. Data Tables **14**, 11 (1974).
[19] L. Wolniewicz and J. D. Poll, Mol. Phys. **59**, 953 (1986).
[20] C. K. Au, G. Feinberg, and J. Sucher, Phys. Rev. A **43**, 561 (1991).
[21] J. M. Taylor, A. Dalgarno, and J. F. Babb, Phys. Rev. A **60**, R2630 (1999).
[22] W. G. Sturrus, E. A. Hessels, P. W. Arcuni, and S. R. Lundeen, Phys. Rev. A **44**, 3032 (1991).
[23] See, for example, Saul T. Epstein, Chem. Phys. Lett. **133**, 276 (1987). In the case of α_s, there appears to be a simple interpretation of this additional energy shift as being due to the fictitious force associated with the acceleration of the H_2^+ ion by the applied electric field. A similar correction, of order ε, occurs in the quadrupole portion of the polarization potential. For this term, no comparable explanation has been found.
[24] A. Dalgarno and J. T. Lewis, Proc. R. Soc. London, Ser. A **233**, 70 (1955).
[25] Richard J. Drachman, Phys. Rev. A **31**, 1253 (1985).
[26] E. A. Hessels, P. W. Arcuni, F. J. Deck, and S. R. Lundeen, Phys. Rev. A **46**, 2622 (1992), and references therein.
[27] A. K. Bhatia and R. J. Drachman, Phys. Rev. A **59**, 205 (1999).
[28] J. Shertzer and C. H. Greene, Phys. Rev. A **58**, 1082 (1998).
[29] R. E. Moss, Chem. Phys. Lett. **311**, 231 (1999).